Chapter 3
Si-nanocrystal-enhanced photoconductive response of silicon-implanted quartz

3.1 Abstract

The Si-nanocrystal-enhanced photoconductivity of a metal-semiconductor-metal photodetector (MSM-PD) made on multi-recipe silicon-ion-implanted and thermal annealed quartz ($SiO_2:Si^+$) substrate is reported. The results of the electrical characteristics show that the annealing-induced leakage current of the $SiO_2:Si^+$ material are strongly related to the nanocrystallite Si (nc-Si). The Al-$SiO_2:Si^+$ contact resistance, contact resistivity and the sheet resistance of $SiO_2:Si^+$ containing the nc-Si structure are determined as 9.1×10^8 Ω, 6.6×10^{10} Ω cm^2, and 3.4×10^{11} Ω/□, respectively. Different carrier transport models are employed to elucidate the nc-Si related current-voltage characteristics. The simulation reveals that the Schottky carrier transport predominated the carrier transport between metal –$SiO_2:Si^+$ interface. The reverse-saturation current (J_s) for the $SiO_2:Si^+$ based MSM-PD is 4.4 pA. The MSM-PD exhibits photocurrent gain of 3 and responsivity of 6.69 nA/W. Wavelength dependent photoconductivity is also observed a maximum photocurrent of 42.6 pA at wavelength of 745 nm.

3.2 Introduction

The strong photoluminescence (PL) from porous Si at room temperature is attracting a new effective way to fabricate Si based visible light emitting materials utilizing nanocrystallite Si (nc-Si), where the band gap is enlarged into visible range, and the quantum confinement effect is thought to be one of main mechanism.[1] Due to the well known disadvantages of porous Si, such as instability, slow electric response, and incompatible technique with microelectronics technology, several efforts have been made to search for other methods, such as Si-ion-implantation into SiO_2, recrystallization of amorphous Si,[2] SiO_2 and Si rf co-sputtering,[3] and chemical vapor deposition from silane[4] Si ions implantation into SiO_2 is of great interest[5-9] because of its many advantages: being routinely used in integrated circuits technology, enhancing the mechanical and thermal stability of materials, and enabling one to rule out some of the alternative luminescence sources such as Si_nH_n compounds as in porous Si.[7]

Many papers reporting visible PL from the Silicon-ion-implanted SiO_2 (SiO_2:Si^+) layers had appeared in the past few years. Much less information has been published until now about electroluminescence (EL) of this layer[10-13] although development of EL structures is the ultimate goal of this research effort. The obvious reason is the inherent low conductivity of SiO_2, preventing an efficient carrier injection. Liao *et al.*[11] studied the EL of SiO_2:Si^+ film as thick as 3000 Å but without heat treatment. They observed a main peak at 2.0 eV

and a shoulder at 1.7 eV under forward voltage higher than 10 V, which denotes a difficult carrier injection. Furthermore, another problem for previous works on $SiO_2:Si^+$ as a light emitting material is the base material of silica glass[5] or thick thermal SiO_2 films[6-9] (thousands of angstroms), which may prevent us from fabricating efficient light emitting diodes.

High-temperature (usually >1000 ^oC) and long-term annealing further leads to the quenching of defect-related PL and to the formation of nc-Si in $SiO_2:Si^+$. The studies on the photocurrent response of $SiO_2:Si^+$ was previously investigated. Choi *et al.*[14] observed a negative photoconductivity in a metal-$SiO_2:Si^+$-Si diode with dense nc-Si under UV illumination. Hirano *et al.*[15] studied the photoconductivity of the Si/SiO_2 multi-layers containing nc-Si with size of 3–5 nm. Coffa *et al.*[16] demonstrated the charge storage and negative photoconductivity of nc-Si embedded in SiO_2/p-Si. These results suggest a strong correlation between the nc-Si and the anomalous photoconductivity.

In this work, the nc-Si enhanced photoconductivity of an inter-digitized metal-$SiO_2:Si^+$-metal photodetector (MSM-PD) made on thermally annealed $SiO_2:Si^+$ substrate is characterized. The experiment results of the nc-Si enhanced photoconductivity are also compared to the simulated result of the theoretical models. The wavelength dependent photoconductivity of the nc-Si MSM-PD and the strong correlation between the nc-Si enhanced photocurrent are reported.

3.3 Experiment

A 1-mm-thick quartz substrate was pre-annealed for 1 hr and concurrently implanted with Si ions at 5×10^{15} ions/cm^2 at 40 keV, 1×10^{16} ions/cm^2 at 80 keV, and 2.5×10^{16} ions/cm^2 at 150 keV. The secondary-ion mass spectroscopy (SIMS) of Si-implanted quartz reveals that the Si atoms with a maximum excess density of 0.8 % are uniformly distributed at depths between 40 nm and 300 nm below the surface, this result agrees quite well with that obtained using TRIM simulation (see the Fig. 3-1).

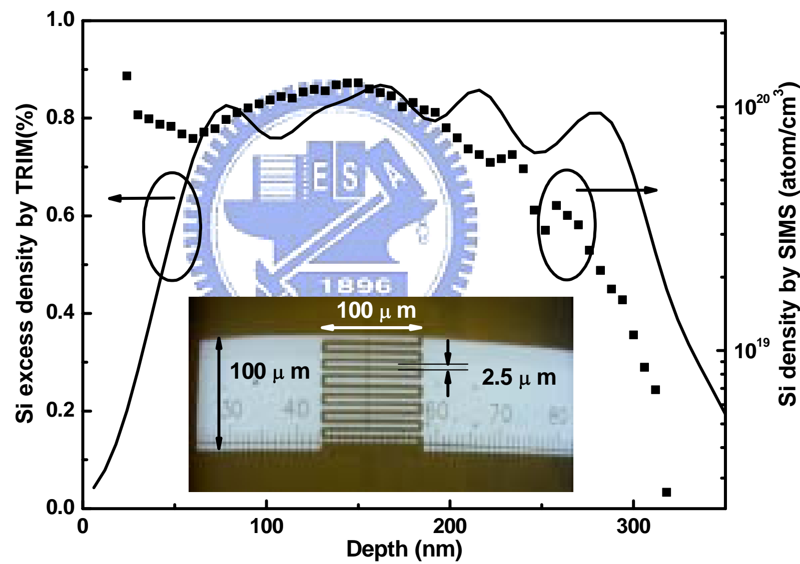

Fig. 3-1 The TRIM-simulated Si excess density as a function of depth. The inset figure illustrates the possible photo-electron transport of the $SiO_2:Si^+$ MSM-PD.

The Si-implanted quartz samples were subsequently annealed at 1100°C in quartz furnace with flowing N_2 gas for 1-3 hrs. Afterwards, and the $SiO_2:Si^+$ MSM-PDs with 500-nm-thick Aluminum Schottky contacts (with 2.5 μm gap spacing) and inter-digitized finger electrodes were fabricated. The finger width and spacing, and the active area of the MSM-PD are 2.5

μm and 100×100 μm^2, respectively (see the inset of Fig. 3-1). The photocurrent was measured using a programmable electrometer (Keithley, model 6517) with resolution as low as 100 fA. A green laser and a Ti:sapphire laser with output power of 10 mW were employed as the illuminating source. The responsivity R of the MSM-PD is calculated using

$$R = \frac{(I_{irr} - I_{dark})}{P_{laser} \cdot (A_{MSM-PD} / A_{laser})}, \tag{3-1}$$

Where I_{irr} and I_{dark} denote the irradiative- and dark- current of the $SiO_2:Si^+$ MSM-PD, A_{laser} is the area of the focused laser spot, A_{MSM-PD} is the active area of the MSM-PD, and P_{laser} is the laser power at the illuminating end.

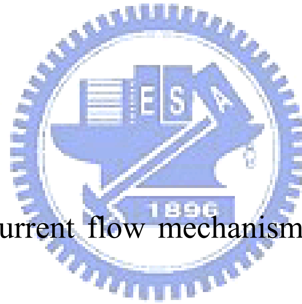

3.4 Theory

There are two main gate current flow mechanisms for the metal-oxide-semiconductor (MOS). The oxide voltage required for one or the other these two mechanisms to occur is shown in Fig. 3-2. In the Fig. 3-2(a), we show the band diagram of an MOS device. The unit of the electron affinity χ is in eV. For $V_{ox} > q\chi$, shown as in Fig. 3-2(b), where V_{ox} is the biased voltage and q is the electron charge, the electrons in the substrate see a triangular barrier and the gate current is due to Fowler-Nordheim tunneling. For $V_{ox} < q\chi$, V_{ox} is approximately 3.2 V for the SiO_2-Si interface. Moreover, the oxide electric field $\varepsilon_{ox}, \varepsilon_{ox} = V_{ox}/t_{ox}$ where t_{ox} is the thickness of oxide layer, must be sufficiently high for tunneling to take place. For oxide thickness of 4-5 nm and above, Fowler-Nordheim (FN)

tunneling is the usual mechanism. For $t_{ox} \leq 3.5$ nm or so, direct tunneling dominates.

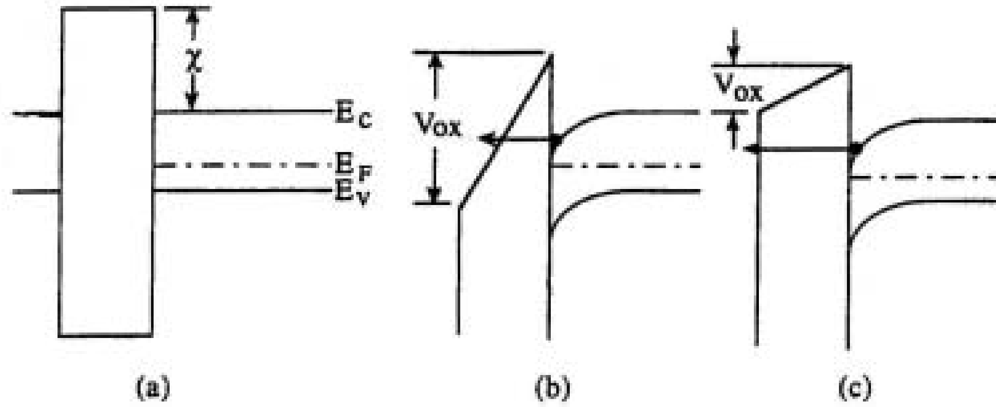

Fig. 3-2 (a) The energy–band diagram of the MOS structure. (b) The illustration of Fowler-Nordheim tunneling. (c) The illustration of direct tunneling.

3.4.1 Fowler-Nordheim Tunneling

FN tunneling is the flow of electrons through a triangular potential barrier. Tunneling is a quantum mechanical process akin to throwing a ball against a wall often enough that the ball goes through the well without damaging the wall or the ball. It also loses no energy during the tunnel event. The probability of this event happening, however, is extremely low, but an electron incident on a barrier typically several nm thick has a high probability of transmission. The FN current density J_{FN} is given by the expreession.[17]

$$J_{FN} = \frac{4\pi qm}{h^3}\int_0^{E_F} dE \int_0^{E} T_t dE_t = A_G A \varepsilon_{ox}^2 \exp(\frac{-B}{\varepsilon_{ox}}), \quad (3\text{-}2)$$

where q is the electronic charge, m is free electron rest mass, h is the Planck' constant,

E_F is the Fermi energy, E_t is the transversal energy component, T_t is the tunneling transmission probability, A_G is the gate area, ε_{ox} the oxide electric field , and A and B are usually considered to be constants. With ε_{ox} in units of V/cm, A and B are given by

$$A = \frac{q^3 (m/m_{ox})}{8\pi h \Phi_B} = 1.54 \times 10^{-6} \text{ (A/V}^2\text{)}, \tag{3-3}$$

$$B = \frac{8\pi\sqrt{2m_{ox}\Phi_B^3}}{3qh} + 6.38 \times 10^7 \text{ (V/cm)}, \tag{3-4}$$

where m_{ox} is the effective mass in the oxide and $\Phi_B = 3.8$ eV is the barrier height at the Si-oxide interface given in units of eV in the expressions for A and B. Φ_B is actually and quantization of electrons at the semiconductor surface. The FN equation is derived under the following assumption: The electrons in the emitting electrode can be described by a free Fermi gas, the electrons in the oxide have a single effective mass m_{ox}, and the tunneling probability is derived by taking into account the component of the electron momentum normal to the interface only.

3.4.2 Direct Tunneling

Direct tunneling is the flow of electrons through the full oxide thickness illustrated in Fig. 3-2(c). The current I_{dur} is given by the expression[18]

$$I_{dir} = A_G A \varepsilon_{ox}^2 \exp\left(\frac{-B\left[1-\left(1-qV_{ox}/\Phi_B\right)^{1.5}\right]}{\varepsilon_{ox}}\right), \tag{3-5}$$

The total gate current is the sum of I_{FN} and I_{dir} with the higher current dominating.

3.4.3 The Schottky barrier model

The current transport of the Schottky barrier model[19] in a metal-semiconductor junction is due to mainly majority carriers as opposed to minority carriers in pn junction. The thermionic emission characteristics are derived by using the assumptions that the barrier height is much larger than kT, so that the Maxwell-Boltzmann approximation applies and that thermal equilibrium is not affected by this process. Fig. 3-3 shows the one-dimensional barrier with an applied forward-bias voltage V_a and shows two electron current density components. The current $J_{s\rightarrow m}$ is the electron current density due to the flow of electrons from the semiconductor into the metal, and the current $J_{m\rightarrow s}$ is the electron current density due to the flow of electrons from the metal into the semiconductor. The subscripts of the currents indicate the direction of electron flow. The conventional current direction is opposite to electron flow.

The net current density in the metal-to-semiconductor junction can be written as

$$J = J_{s\rightarrow m} - J_{m\rightarrow s}, \tag{3-6}$$

which is defined to be positive in the direction from the metal to the semiconductor. We find that

$$J = \left[A^* T^2 \exp\left(\frac{-e\Phi_{Bn}}{kT} \right) \right] \left[\exp\left(\frac{eV_a}{kT} \right) - 1 \right], \tag{3-7}$$

where

$$A^* \equiv \frac{4\pi e m^* k^2}{h^3}, \tag{3-8}$$

The parameter A^* is called the effective Richardson constant for thermionic emission, T is the temperature (K), e is the electronic charge and Φ_{Bn} is schottky barrier height.

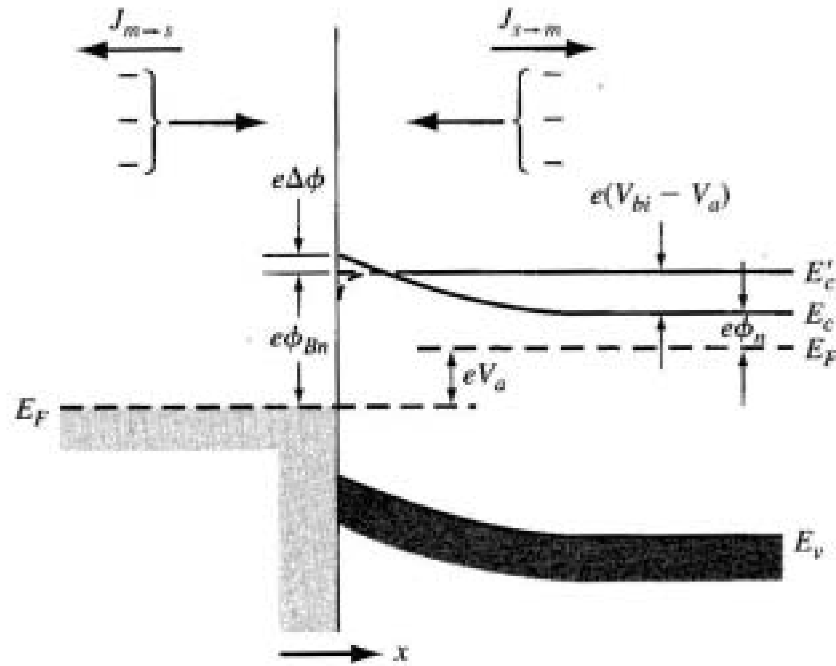

Fig. 3-3 The energy-band diagram of forward-biased metal-semiconductor junction.

Equation (6) can be written in the usual diode form as the net current density

$$J = J_{ST} \left[\exp\left(\frac{eV_a}{kT} \right) - 1 \right], \tag{3-9}$$

where J_{ST} is the reverse-saturation current density and is given by

$$J_{ST} = \left[A^* T^2 \exp\left(\frac{-e\Phi_{Bn}}{kT} \right) \right], \tag{3-10}$$

3.4.4 Transmission-Line-Model (TLM)

The TLM structure, used for planar contact-resistance measurements, is a series of identical ohmic contacts, of width w and length l_c, spaced at varying intervals l_1, l_2, l_3, l_4,…, as shown in Fig. 3-4 (a).

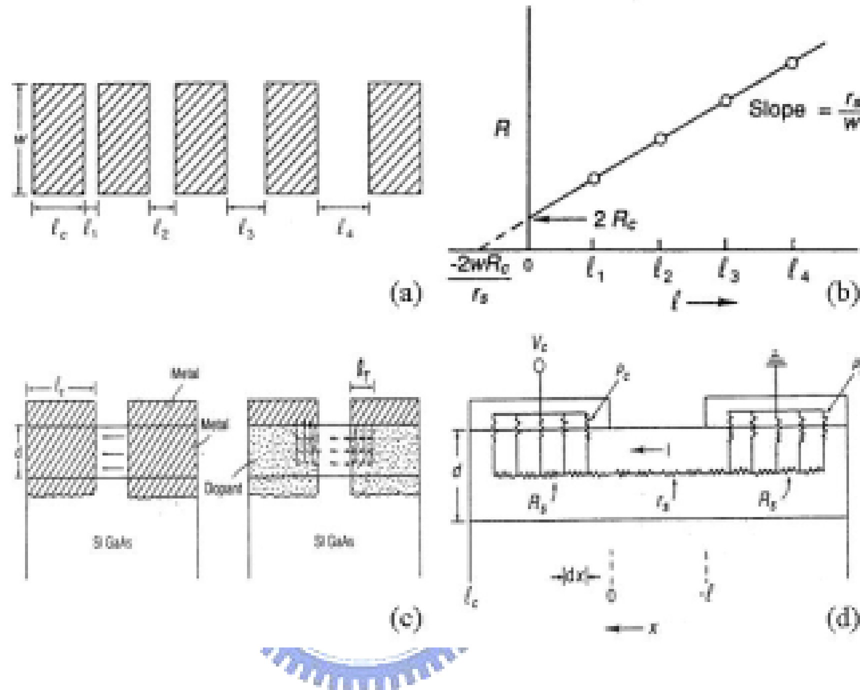

Fig. 3-4 (a) A standard TLM contact-resistance pattern. (b) the expected resistance R as a function id contact-spacing l_i. (c)Two possible scenarios for ohmic metal contacts on the surface of a semiconductor layer. (d) A transmission-line-model equivalent circuit for current flow in a thin-layer semiconductor device.

If a voltage is impressed between two of these constant, separated by l_i, then the toltal resistance, R=V/I, will consist of two components:

$$R = 2R_c + r_s \frac{l_i}{w}, \qquad (3\text{-}11)$$

where, R_c is the resistance due to a single contact and r_s is the sheet resistance of the semiconductor material between the contacts. If R is now plotted vs. l_i, as shown in Fig. 3-4 (b), then the slope of the resulting line will be r_s/w, and the intercept, $2R_c$. Thus, the

TLM structure provides some very useful information, including the normalized contact resistance $r_c=R_c/w$, which is an important figure of merit for circuit designers. Note that the current 'appears' to be coming from a point $2R_cw/r_s$ from the edge of the contact, since R extrapolates to zero at that point. If r_s is also the sheet resistance of the material under the contact, then the intercept is just twice a quantity known as the transfer length, which will be discussed later.

Although r_c is a useful quantity, it tells us nothing about the actual metal/semiconductor (M/S) barrier resistance because it is not clear just what portion if the metal area is being used to transfer the current. For example, consider the situation in Fig. 3-4(c), in which the metal has completely diffused through the active layer of thickness d. Then the current flows uniformly out of a contact area wd, and the specific contact resistivity is $\rho_c=R_cwd$. However, it would rarely ever be true that the contact metal would diffuse in such a manner; more probably, it would remain nearly planar, as shown in Fig. 3-4(c), but with some elements diffusing partially into the semiconductor below.

Consider the distributed resistance circuit of Fig. 3-4(d). A current I(0), flowing from right to left, enters the left-hand contact region at x = 0 and floes horizontally under the contact, with various portions being lost through the infinitesimal vertical resistors $\rho_c/w\ dx$ until I(0) is fully exhausted. It is assumed that the layer thickness d is small enough that the current density does not vary significantly over the cross section wd. Then, in the

region $0 \le x \le l_c$, r\the circuit can be described by the following differential equations:

$$dV(x) = -\frac{R_s}{w} I(x)dx, \tag{3-12}$$

$$dI(x) = \frac{w}{\rho_c}[V_c - V(x)]dx, \tag{3-13}$$

where V_c would have to be negative in Fig. 3-4(d) for the conventional current to flow as shown. Here ρ_c is the specific contact resistivity of the M/S barrier, and R_s is the sheet resistance of the material under the contact. It is important to note that, in general, $R_s \neq r_s$, where the latter quantity is the sheet resistance in the bulk region. By differentiating Eq. (12), and then substituting Eq. (13), a second-order differential equation is obtained.

$$V''(x) - k^2 V(x) = -k^2 V_c, \tag{3-14}$$

where $k^2 \equiv R_s/\rho_c$. This solution is

$$V(x) = V_c + [V(0) - V_c]\cosh(kx) + \frac{V'(0)}{k}\sinh(kx), \tag{3-15}$$

Since no current can flow out of the end of the contact, we must have $I(l_c)=0$. Therefore, from Eq. (13),

$$0 = I(l_c) = -\frac{w}{R_s}V'(x) = -\frac{w}{R_s}\left\{k[V(0) - V_c]\sinh(kl_c) - \frac{R_s I(0)}{w}\cosh(kl_c)\right\}, \tag{3-16}$$

where we have also substituted $V'(0)=-R_s I(0)/w$. The contact resistance is now defined as

$$R_s = \frac{V(0) - V_c}{I} = \frac{V(0) - V_c}{I(0)} = \frac{R_s}{wk}\coth(kl_c) = \frac{\sqrt{R_s \rho_c}}{w}\coth(kl_c), \tag{3-17}$$

Equation (17) is widely employed in contact-resistance studies. Typically, $R_s \cong 10^2$ Ω/□, and $\rho_c \cong$ Ω-cm^2, so that $k \cong 10^4$ cm^{-1}; then if $l_c > 2$ μm=2×10^{-4} cm, $kl_c \ge 2$, and $\coth(kl_c) \ge 2$

specifies electrically long contact, and nearly always hold in practice; then $R_c = \sqrt{R_s \rho_c} / w$,

or $\rho_c \cong \dfrac{w^2 R_c^2}{R_s}$ (3-18)

Also, $l_T = wR_c / R_s = \sqrt{(\rho_c / R_s)}$, so that the current is all transferring to or from the metal within a distance if about 1 μm from the inside edge. Thus, the effective contact area of a planar contact is approximately (wl_T) instead of wl_c.

3.5 Results and Discussion

3.5.1 The characteristics of the electrical properties of $SiO_2:Si^+$

The dark currents of $SiO_2:Si^+$ material with TLM patterns made on the $SiO_2:Si^+$ and pure quartz substrates were measured at different biased voltage. Figure. 3-5 shows the Schottky diode with 2.5 μm gap spacing made on pure quartz, as-implanted $SiO_2:Si^+$ and $SiO_2:Si^+$ substrates annealed at 1100°C for 1 hr and 3 hrs. The pure quartz, as-implanted $SiO_2:Si^+$ substrate and $SiO_2:Si^+$ sample annealed at 1100°C for 1 hr exhibit the closely insulating property. That is, the dark current lower than 1 pA. After annealing 3 hrs, the dark current at biased voltage of 10 achieves 445.2 pA. According the current–voltage (I-V) characteristic of the $SiO_2:Si^+$, the $SiO_2:Si^+$ exhibits the property of semiconductor. By the calculation of the TLM method shown in Fig. 3-6, the resistance due to a single contact (R_c) is 9.1×10^8 Ω, the sheet resistance of the semiconductor material between the contacts (r_s) is

3.4×10^{11} Ω/□ and the specific contact resistivity (ρ_c) is 6.6×10^{10} Ω cm^2. Furthermore, the electrons transported model should be clearly defined.

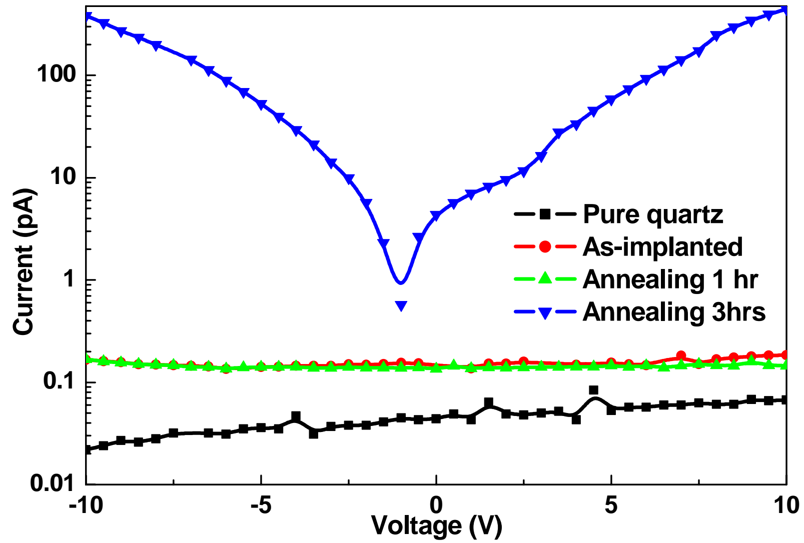

Fig. 3-5 The current-voltage curve for Schottky diodes with 2.5 μm gap spacing made on pure quartz, as-implanted, annealed at 1100°C for 1 hr and 3 hrs.

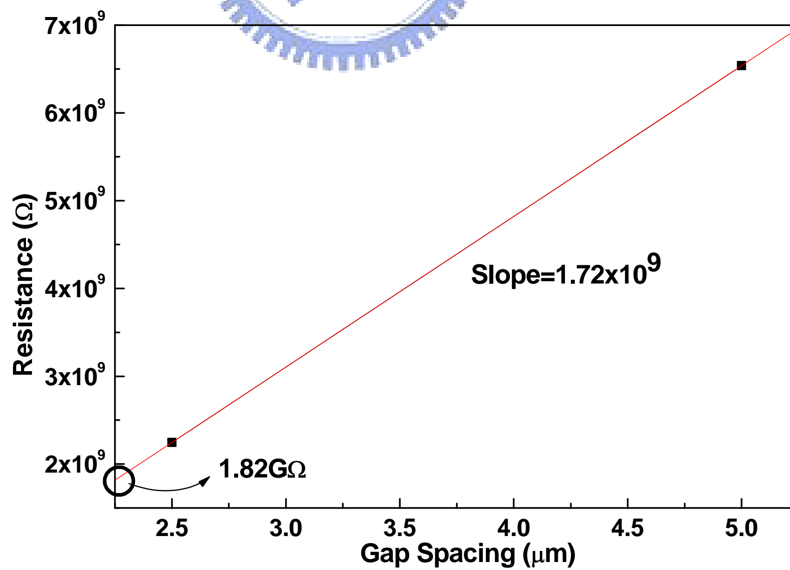

Fig. 3-6 The result of TLM diode of SiO_2:Si^+ as a function of different applied gap spacing.

There are two main gate current flow mechanisms for the metal-oxide-semiconductor

(MOS). However, in this work the structure of the sample is metal-oxide-semiconductor-oxide-metal (MOSOM). The two main gated current flow mechanisms for the single MOS structure are not satisfied and should be corrected. The simulations of the MOSOM structure by the Schottky model, FN tunneling model and direct tunneling model are obtained. The tunneling transmission probability can be calculated due to two situations for MOSOM. First situation is that the electrons tunnel from metal to semiconductor. Another situation is that the electrons tunnel from semiconductor to metal. In the beginning of the simulation, the F-N tunneling current density was corrected to

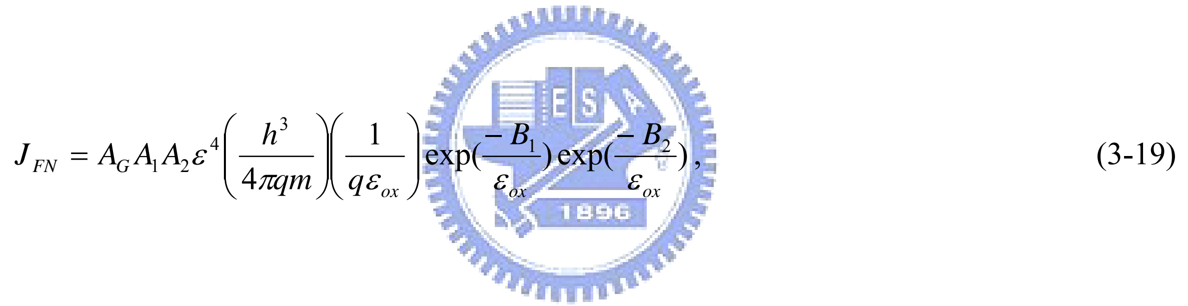

$$J_{FN} = A_G A_1 A_2 \varepsilon^4 \left(\frac{h^3}{4\pi qm}\right)\left(\frac{1}{q\varepsilon_{ox}}\right)\exp\left(\frac{-B_1}{\varepsilon_{ox}}\right)\exp\left(\frac{-B_2}{\varepsilon_{ox}}\right), \quad (3\text{-}19)$$

where A_1 and B_1 are the constant for the metal tunneling to semiconductor, and A_2 and B_2 are the constant for the semiconductor tunneling to metal. However, the direct tunneling corrected to

$$J_{dir} = A_G A_1 A_2 \varepsilon^4 \left(\frac{h^3}{4\pi qm}\right)\left(\frac{1}{q\varepsilon_{ox}}\right)\exp\left(\frac{-B_1\left[1-\left(1-qV_{ox}/\Phi_{B1}\right)^{1.5}\right]}{\varepsilon_{ox}}\right)\exp\left(\frac{-B_2\left[1-\left(1-qV_{ox}/\Phi_{B2}\right)^{1.5}\right]}{\varepsilon_{ox}}\right), \quad (3\text{-}20)$$

where the Φ_{B1} is the barrier height at Al-oxide interface and Φ_{B2} is the barrier height at Si-oxide interface. The Schottky carrier transported model for MSM structure is also

considered and the simulated results the gated current flow mechanism are also shown in Fig 3-7.

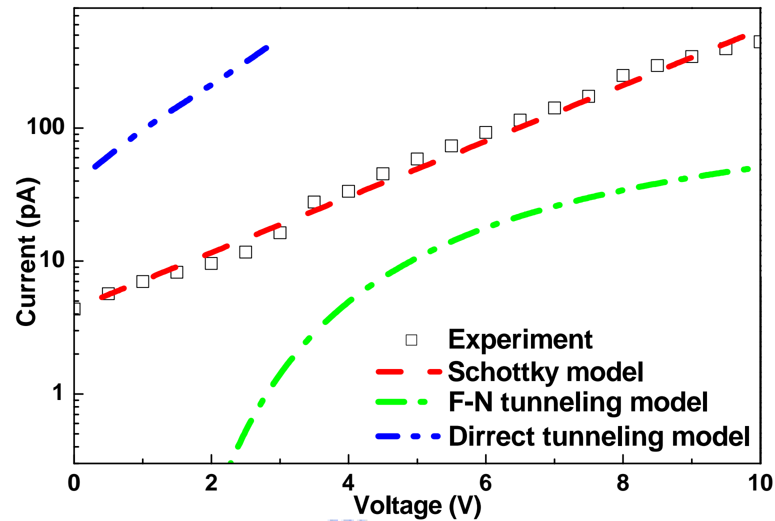

Fig. 3-7 Compared experiment with simulation due to Fowler-Nordheim tunneling, direct tunneling and Schottky barrier model.

According to the results of experiments and simulations, the two main gated current flow mechanisms for the MOSOM are not satisfied with those of electrical properties of $SiO_2:Si^+$ containing nc-Si. However, the simulation of the Schottky carrier transported model can prove that the $SiO_2:Si^+$ with the nc-Si structure has the characteristic of semiconductor and the reverse-saturation current is 4.4 pA.

3.5.2 Measurement of photocurrent of $SiO_2:Si^+$ with nc-Si structure

The analysis of the irradiative current of a MSN-PD with thirteen-interdigitated-electrodes fabricated on $SiO_2:Si^+$ substrate is performed. The I-V curves for dark and luminescent condition under the injection power of 10 mW at 532 nm for the pure quartz were shown in Fig. 3-8.

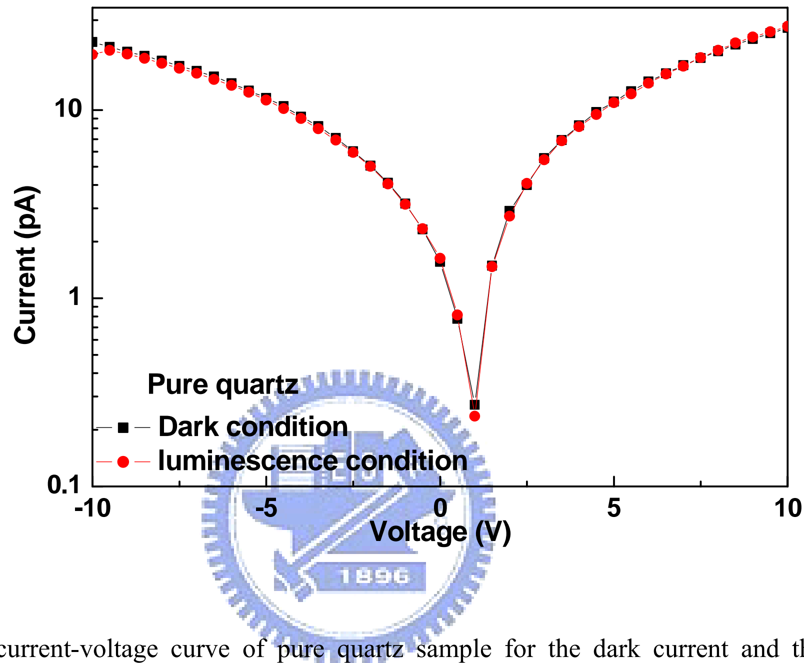

Fig. 3-8 The current-voltage curve of pure quartz sample for the dark current and the irradiative current.

At bias of 10 volts, the dark current and irradiative current are 27.3 pA and 27.8 pA, respectively, which correspond to a photocurrent gain (I_{irr}/I_{dark}) of 1 and a responsivity of 50 pA/W. After implantation, the dark current and the irradiative currents at biased voltage of 10 V are 23.8 pA and 24.1 pA, respectively (see the Fig. 3-9), which correspond to the photocurrent gain of 1 and a responsivity of 50 pA/W for the as-implanted $SiO_2:Si^+$ sample. After 1-hr annealing, the dark current and irradiative current are 20.4 pA and 20.5 pA, respectively (see the Fig. 3-10), which correspond to photocurrent gain of 1 and a responsivity

of 10 pA/W for the $SiO_2:Si^+$ sample.

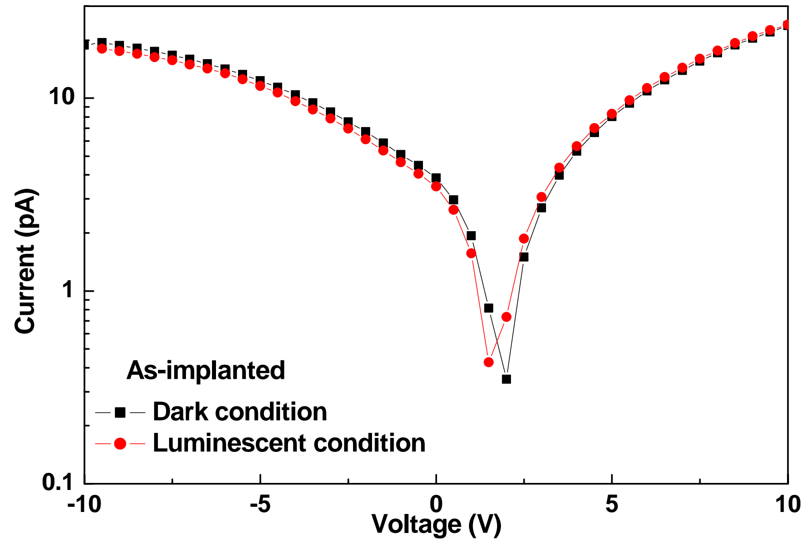

Fig. 3-9 The current-voltage curve of as-implanted sample for the dark current and the irradiative current.

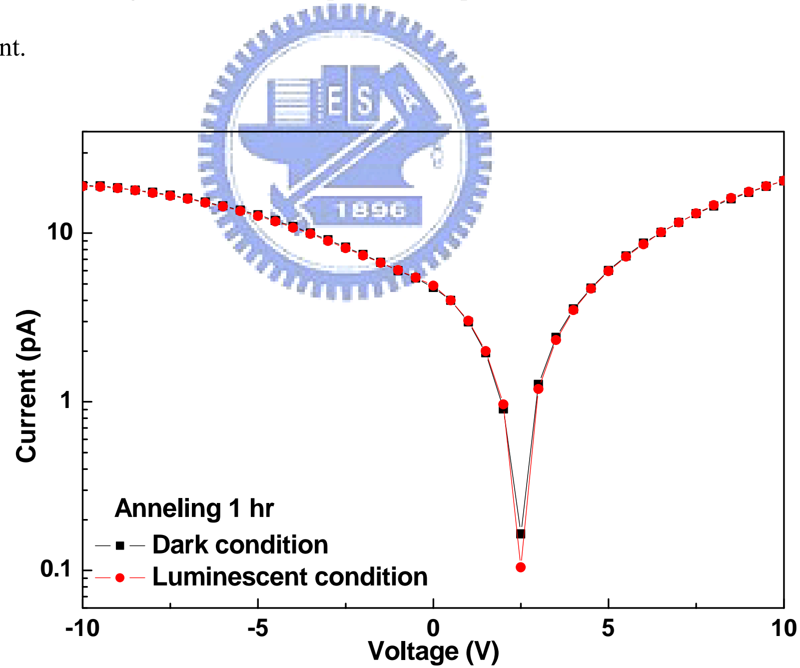

Fig. 3-10 The current-voltage curve of 1-hr annealing sample for the dark current and the irradiative current.

However, after 3-hrs annealing, the dark current at biased voltage of 10 V and the irradiative current are 32.8 pA and 100 pA, respectively (see the Fig. 3-11), which correspond

to the photocurrent gain of 3 and a responsivity of 6.70 nA/W for the $SiO_2:Si^+$ sample. Furthermore, the relationship between the photocurrent and biased voltage was shown in Fig. 3-12 and the maximum photocurrent was 67 pA at the biased voltage of 10. In the Fig. 3-13, the relationship between the responsivity and photocurrent in different condition was visibly observed the high responsivity.

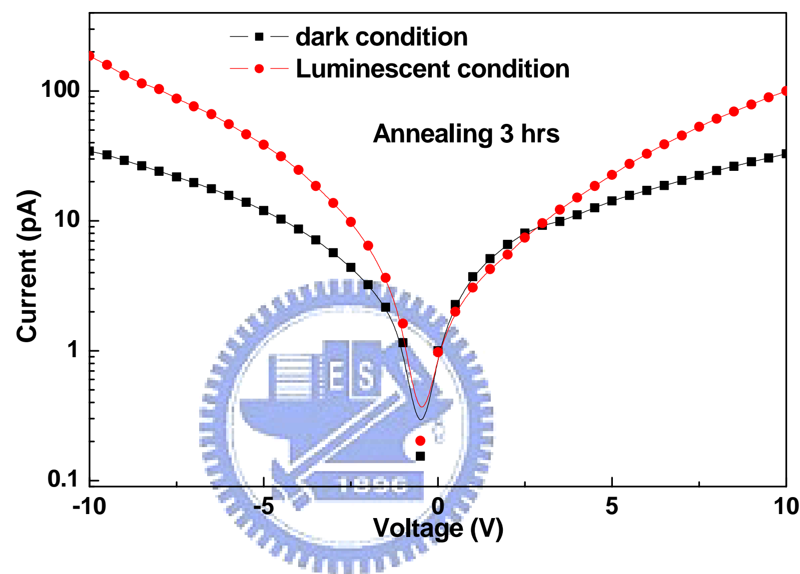

Fig. 3-11 The current-voltage curve of 3-hr annealing sample for the dark current and the irradiative current.

The phenomenon proved that more carriers with large kinetic energies can be tunneled through the nc-Si due to the irradiative excitation.

By illuminating with the Ti:sapphire laser, the photocurrent response of the nc-Si MSM-PD as a function of biased voltage can be obtained. It is seen that the current response of the nc-Si MSM-PD is significantly enhanced under the photo-illuminated process. Under the illuminated power and wavelength of 10 mW and 750 nm, the irradiative current of the

$SiO_2:Si^+$ diode at the biased voltage of 10 is about 7.4 pA, which is larger than the result of the dark current at the same biased voltage.

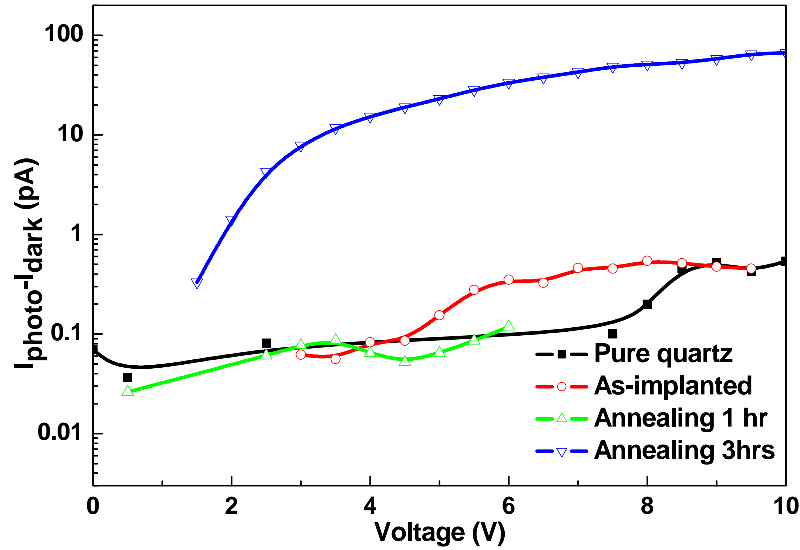

Fig. 3-12 The relationship between photocurrent and bias voltage.

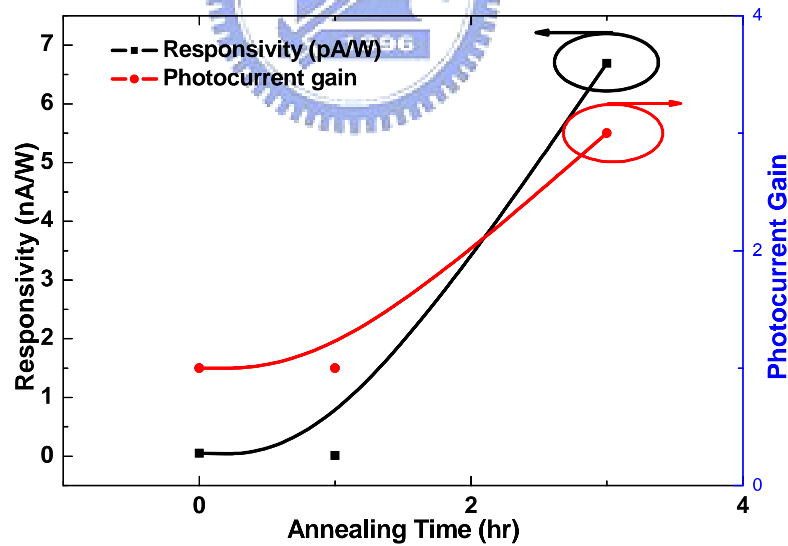

Fig. 3-13 The relationship between the responsivity and photocurrent in different condition.

In addition, the photocurrent response can be further improved by the shorter-wavelength illuminating laser and the results are shown in Fig. 3-14. Under illuminated power and

wavelength of 10 mW and 745 nm, the irradiative current of the nc-Si MSM-PD is about 42.6 pA, which is also larger than the dark current at the biased voltage of 10.

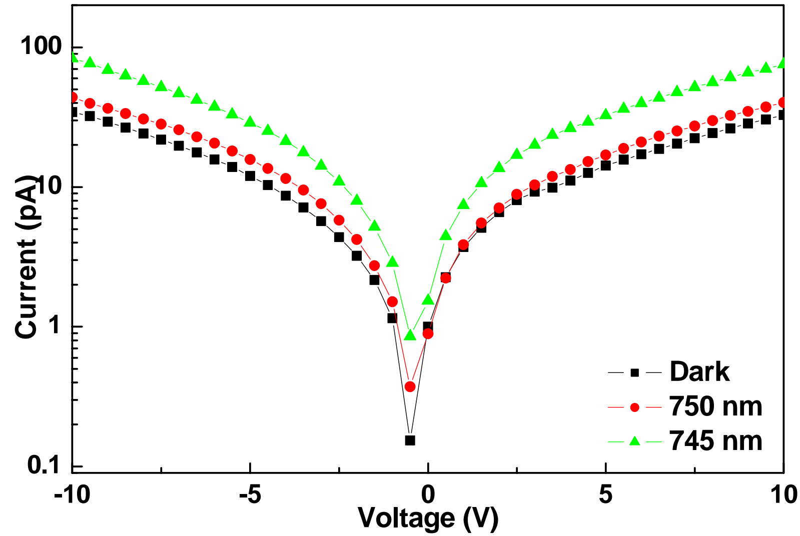

Fig. 3-14 The irradiative current of $SiO_2:Si^+$ with MSM-PD due to different wavelength source.

Furthermore, the wavelength dependence of the measurement photocurrent is shown in Fig. 3-15. The maximum value of photocurrent of the nc-Si MSM-PD is 42.6 pA at the wavelength of 745 nm. The explanation of the improved photocurrent response at nc-Si band gap is primarily attributed to larger absorption coefficient.

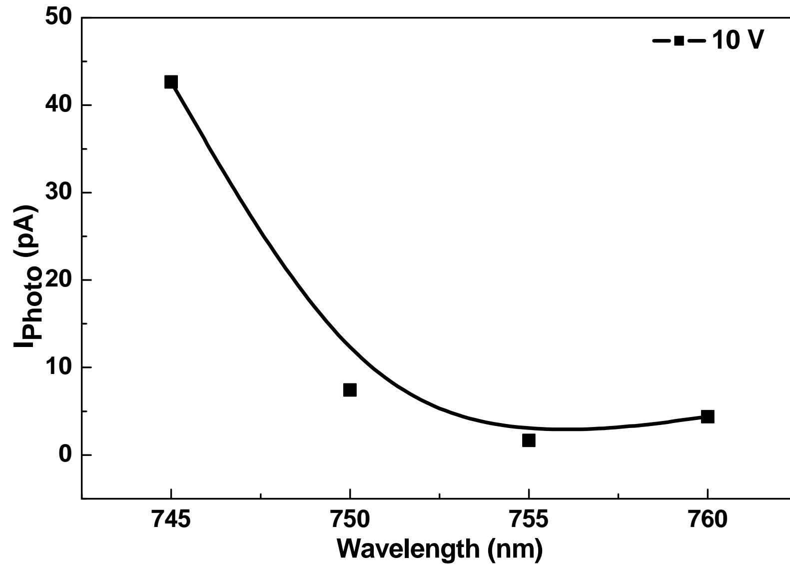

Fig. 3-15 The wavelength dependence of the photocurrent incident power 25 mW for $SiO_2:Si^+$ MSM-PD.

3.6 Conclusion

In conclusion, the results of nc-Si enhanced photoconductive response of multi-recipe $SiO_2:Si^+$ are performed. After 3-hr annealing, the maximum intensity of PL spectrum at the wavelength of 754 nm, corresponding to a size diameter of nc-Si about 4 nm, was observed. For the electrical properties of $SiO_2:Si^+$, the gated current flow mechanisms and photoconductivity of an inter-digitized MSM-PD made on high-temperature annealed $SiO_2:Si^+$ substrate are reported. According to the TLM model, the resistance due to a single contact (R_c) is 9.1×10^8 Ω, the sheet resistance of the semiconductor material between the contacts (r_s) is 3.4×10^{11} Ω/□ and the specific contact resistivity (ρ_c) is 6.6×10^{10} $\Omega\,cm^2$. However, the gated current flow mechanisms show that two main gated current flow

mechanisms for the MOSOM are not satisfied with nc-Si structure but the simulation of the Schottky carrier transported model is proved that the nc-Si structure has the characteristic of semiconductor and the reverse-saturation current is 4.4 pA. The photoconductivity of MSM-PD shows that the gain of photocurrent is 3 and the responsivity is 6.69 nA/W for the nc-Si structure and by wavelength dependence the maximum value of photocurrent of the nc-Si MSM-PD is 42.6 pA at the wavelength of 745 nm. That explanation of the improved photocurrent response at nc-Si band gap is primarily attributed to larger absorption coefficient.

References

[1] L. T. Canham, Appl. Phys. Lett. **57**, 1046 (1990).

[2] X. Zhao, O. Schoenfeld, J. Kusano, Y. Aoyagi, and T. Sugano, Jpn. J. Appl. Phys. Part 2 **33**, L649 (1994).

[3] Q. Zhang, S. C. Bayliss, and R. A. Hutt, Appl. Phys. Lett. **66**, 1977 (1995).

[4] S. Tong, X. N. Liu, and X. M. Bao, Appl. Phys. Lett. **66**, 469 (1995).

[5] T. Shimizu-Iwayama, K. Fujita, S. Kakao, K. Saitoh, T. Fujita, and N. Itoh, J. Appl. Phys. 75, 7779 (1994).

[6] T. Simizu-Iwayama, S. Nakao, and K. Saitoh, Appl. Phys. Lett. **65**, 1814 (1994).

[7] P. Mutti, G. Ghisloti, S. Bertoni, L. Bonoldi, G. F. Cerofolni, L. Meda, E. Grilli, and M. Guzzi, Appl. Phys. Lett. **66**, 851 (1995).

[8] T. Komoda, J. Kelly, F. Cristiano, A. Nejim, P. L. F. Hemment, K. P. Homewood, R. Gwilliam, J. E. Mynard, and B. J. Sealy, Nucl. Instrum. Methods Phys. Res. B **96**, 387 (1995).

[9] L. S. Liao, X. M. Bao, X. Q. Zheng, N. S. Li, and N. B. Min, Appl. Phys. Lett. **68**, 850 (1996).

[10] K. V. Shcheglov, C. M. Yang, K. J. Vahala, and H. A. Atwater, Appl. Phys. Lett. **66**, 745 (1995).

[11] L. S. Liao, X. M. Bao, N.S. Li, X. Q. Zheng, and N.B. Min, Solid State Commun. **97**,

1039 (1996).

[12] H. Z. Song, X. M. Bao, N. S. Li, and J. Y. Zhang, J. Appl. Phys. **82**, 4028 (1997).

[13] L. Rebohle, J. von Borany, R. A. Yankov, W. Skorupa, I. E. Tyschenko, H. Frob, and K. Leo, Appl. Phys. Lett. **71**, 2809 (1997).

[14] S. H. Choi and R. G. Elliman, Appl. Phys. Lett. **74**, 3987 (1999).

[15] Y. Hirano, F. Sato, S. Aihara, N. Saito, S. Miyazaki, and M. Hirose, Appl. Phys. Lett. **79**, 2255 (2001).

[16] S. Coffa, A. Polman, and O. Soref, Mat. Res. Soc. Symp. Proc. **486**, (1998).

[17] M. Lenzlinger and E. H. Snow, J. Appl. Phys. **40**,278 (1969).

[18] K. F. Schuegraf and C. M. Hu, Semicond. Sci. Technol. **9**, 989 (1994).

[19] D. A. Neamen, Semiconductor Physics and Devices Basic Principles, 3rd ed. (University of New Mexico,2003), pp. 337-339.